Surface & Coatings Technology 205 (2010) 759–765

Contents lists available at ScienceDirect

Surface & Coatings Technology

journal homepage: www.elsevier.com/locate/surfcoat

Influence of alloy chemistry on microstructure and properties in NiCrBSi overlay coatings deposited by plasma transferred arc welding (PTAW)

T. Liyanage [a], G. Fisher [b], A.P. Gerlich [a,*]

[a] Department of Chemical and Materials Engineering, University of Alberta, Edmonton, AB, Canada T6G 2V4
[b] Alberta Innovates – Technology Futures, 250 Karl Clark Rd, Edmonton, AB, Canada T6E 0P3

ARTICLE INFO

Article history:
Received 27 October 2009
Accepted in revised form 28 July 2010
Available online 3 August 2010

Keywords:
NiCrBSi
Overlay
PTAW
Microstructure
Hardness
EPMA
AES

ABSTRACT

The microstructures and performance of two NiCrBSi alloy overlays deposited by plasma transferred arc welding are studied. The coatings consist of a γ-Ni primary dendritic phase with harder Ni + Ni_3B or Ni + Ni_3Si eutectics and Cr-based particles (CrB, Cr_3C_2, and Cr_7C_3) situated at the interdendritic regions. It was found that the volume fraction of the soft primary dendritic phase drastically decreased and the proportion of chromium borides and carbides increased with an increase of C, B, Si, and Cr content. Microhardness testing revealed that the primary Ni dendrite, interdendritic, and Cr-particle phases had average hardness values of 405, 860, and 1200 HV respectively. An increase in the volume fraction of hard eutectics and Cr-particles lead to a substantial increase in hardness and wear resistance.

1. Introduction

Overlay welding is used to improve the wear resistance of surfaces on industrial parts by depositing a protective layer of abrasion and/or corrosion resistant weld metal onto a base material surface. This technique is especially useful in high wear environments such as those experienced in a wide range of mining industries. Since extreme wear decreases productivity and the useful life of equipment, overlay welding is used to apply a thick coating onto components in order to reduce the overall maintenance costs [1]. Since the coating may also be applied with metal arc welding techniques in the field, this is especially advantageous when refurbishing high-cost equipment. The NiCrBSi family of alloys has been originally developed for high velocity oxyfuel (HVOF) thermal spray coating applications where excellent wear resistance is a primary requirement [2]. However, plasma transferred arc welding (PTAW) may also be used to deposit this alloy, offering high deposition rates (up to 15 kg/h), good deposition efficiency (about 85%), and low dilution of the substrate material [3].

Previous findings have shown that NiCrBSi coatings deposited by HVOF are comprised of a γ-Ni solid solution with small amounts of Ni_3B and CrB phases [4]. Laser cladding has also been shown to produce a deposit containing a dendritic Ni-rich phase with a metastable Ni_3B eutectic [5] and interdendritic phase with Ni–Si laminar eutectics, and precipitates suggested to consist of CrB and Cr_3C_2 or $(Cr,Fe)_7C_3$ [5]. In deposits produced using PTAW, the phases found included a γ-Ni phase, with Cr_2B, Cr_3C_2 and Cr_7C_3 particles [3]. PTAW deposits made using two NiCrBSi alloys with differing Cr contents (from 10 to 12%) consisted of a γ-Ni dendritic phase and interdendritic precipitates which were found to be a boron-rich dark blocky phase, elongated C and Cr-rich phase (Cr-carbide), and a Cr and B-rich flower-like phase (Cr-boride) [6]. The addition of Cr, B, and C increased the fraction of these phases and resulted in an increase the erosion–corrosion resistance by 20% during slurry wear testing, since the low-Cr alloy consisted of coarser columnar dendrites with much smaller carbides and silicides [6]. In addition, XRD analysis of plasma sprayed deposits showed that these consisted mainly of γ-Ni, $(Cr,Fe)_7C_3$, CrB and Ni_3B [7].

The deposition method not only influences the microstructures produced, but also the mechanical properties of the deposit. For example coatings had hardness values ranging from 7.7 to 4.5 GPa (measured by nanoindentation) when different combinations of flame-spraying and laser cladding are used [5]. The microstructural features in laser clad coatings produced wear rates which were half of those produced by flame-spraying [5].

A wide range of NiCrBSi alloy chemistries are available which yield various degrees of hardness and wear resistance, however there is a limited understanding of the correlation between the composition, microstructure and properties of these materials. These alloys have been largely developed for oxyfuel and other thermal spraying processes where the peak temperatures are limited, and so the

* Corresponding author. Department of Chemical and Materials Engineering, University of Alberta, 7-036 ECERF Building, 9107 – 116 Street, Edmonton, AB, Canada T6G 2V4. Tel.: +1 780 492 8853; fax: +1 780 492 2881.
E-mail address: gerlich@ualberta.ca (A.P. Gerlich).

0257-8972/$ – see front matter © 2010 Elsevier B.V. All rights reserved.
doi:10.1016/j.surfcoat.2010.07.095

formation of low melting point phases (such as eutectics involving Ni_3B and Ni_3Si) are desired. However, this is not necessarily a requirement for the PTAW process since temperatures of >20,000 K are readily produced within the constricted arc [8]. As such, there is a need to reassess the role of melting point suppressing elements, such as B and Si [9] during PTAW of these alloys. In the present work, the microstructures and properties in two commercial NiCrBSi alloys are examined with similar Cr content in order to determine the influence of other alloying constituents. Quantitative microscopy is used to compare the volume fractions of various phases, and this is correlated to the properties of the coatings.

2. Experimental

The two NiCrBSi alloy powders used during PTAW deposition had the nominal compositions shown in Table 1. The coatings were applied with PTAW parameters as follows: arc voltage of 25 V, current of 140 to 150 A (in DC electrode negative polarity), powder feed rate of 25 g/min, Ar gas shielding at a flow rate of 12 l/min, 14 mm working distance, and a travel speed of 0.6 mm/s. Optical microscopy was conducted following etching with Marble's reagent. Scanning electron microscopy (SEM), energy-dispersive X-ray (EDX) spectroscopy, electron probe microanalysis (EPMA) with wavelength dispersive spectroscopy (WDS), and Auger Electron Spectroscopy (AES) were used to characterize the microstructures of the deposits.

Calculation of the dendrite and interdendrite area fractions were performed on the EPMA images using Adobe Photoshop CS4 software. For example, to calculate the particle fraction, the image colours were first inverted, a threshold value was chosen which isolated the particles and the area was then calculated by the measurement function. A similar method (without inverting colours) was used to calculate the dendrite fraction. The dendrite and particle areas were extracted from the images and the interdendritic fraction was taken as the difference between the total area and the sum of the dendrite and particle areas.

Vickers microhardness was conducted using a Mitutoyo MVK-H1 with a 1 kg load to determine the average hardness through the coating thickness, and a 25 g load to measure the hardness of specific phases. Unless otherwise noted, hardness values reported for a specific phase represent an average of at least 5 indentations.

3. Results

3.1. Optical and SEM microscopy

PTAW overlays were 5 to 6 mm in thickness with no observed porosity in optical micrographs. Alloy A contained large dendrites of γ-Ni phase, along with fine particles in the interdendritic regions, see Fig. 1(a). In Alloy B, the γ-Ni phase dendrites were much finer and more difficult to discern, and a significantly larger fraction of blocky, globular, and rhombus-shaped particles could be observed in the interdendritic regions. The microstructure of Alloy A is shown using SEM in Fig. 2, and EDX analysis was used to quantify the composition of hardness indents (Table 2). For example the chemistry at the cores of the γ-Ni dendrites in Alloy A (e.g. point 1 in Fig. 2) as well as the interdendritic regions (e.g. points "2" and "3" in Fig. 2) were determined. Several Cr-rich particles could also be detected in the interdendritic regions of Alloy B as indicated in Fig. 2, however EDX

Table 1
Nominal compositions of alloys studied.

	Fe wt.%	B wt.%	C wt.%	Si wt.%	Cr wt.%	Ni wt.%
Alloy A	2.2	1.4	0.3	3.2	7–9	Balance
Alloy B	3–4	1.8–2.3	0.45	4	10.5	Balance

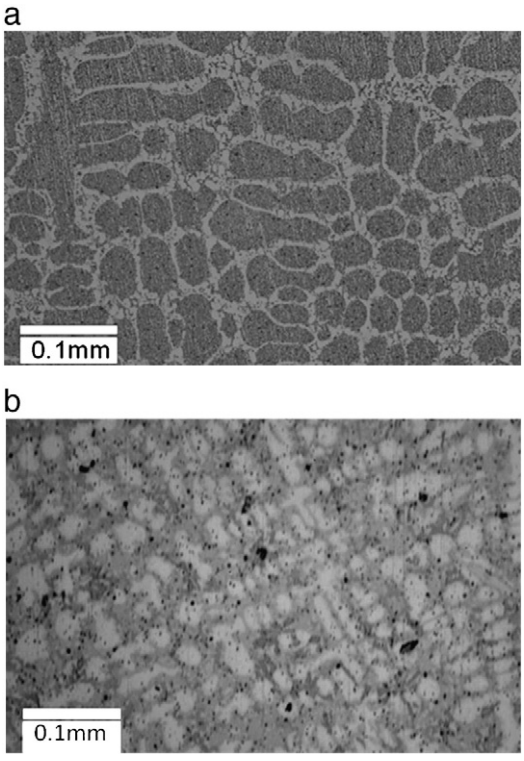

Fig. 1. Optical micrographs of (a) Alloy A, and (b) Alloy B.

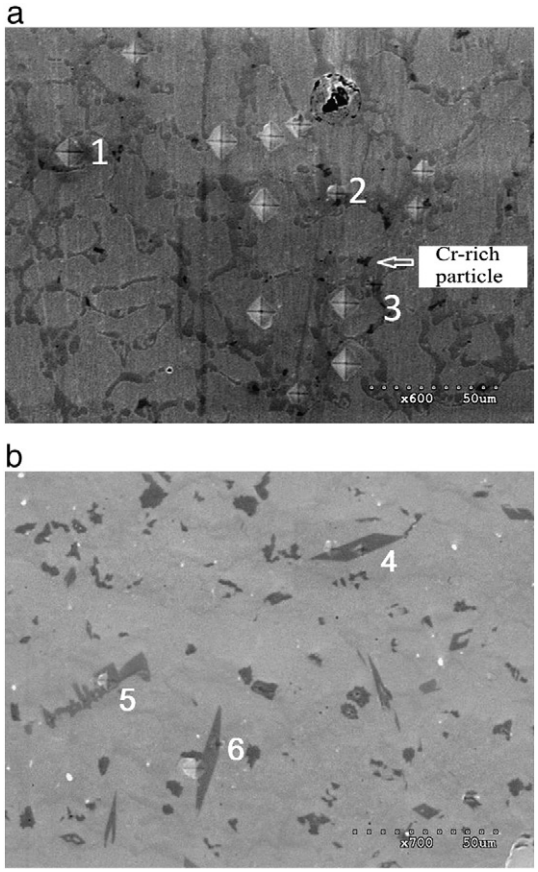

Fig. 2. (a) SEM image of selected area of Alloy A. (b) SEM image of selected area of Alloy B.

Table 2
EDX point quantification of locations in Fig. 2, all in wt.%.

Location	Ni	Cr	C	Fe	Si
1	85.5	9.6	0.0	3.1	1.8
2	88.6	7.3	0.0	1.6	2.5
3	83.6	9.6	0.0	1.5	5.3
4	17.5	57.5	22.7	1.0	1.3
5	38.1	42.7	13.0	3.7	2.4
6	10.0	65.3	23.3	0.9	0.6

could not be used to conclusively identify particles containing carbon or boron due to the limitations of the detector, and hence these phases were subsequently identified by a combination of EPMA and AES.

EDX analysis of Alloy B in the interdendritic region is shown in Fig. 3. The fraction of γ-Ni phase is much lower in Alloy B, and a number of Cr-carbides could be distinguished within the interdendritic regions. EDX analysis of Alloy B showed that the precipitates ("4", "5", and "6" in Fig. 2) were chromium carbides with varying Cr to C ratios, suggesting these may correspond with different phases. The interdendritic regions of both alloys appeared to contain a globular eutectic structure, see Fig. 3. EDX analysis indicates that the component with lower atomic contrast is enriched in Si. A low-Cr content was measured in the interdendritic regions where no particles are present, see Fig. 3. As mentioned earlier, since EDX cannot detect boron in particular, these regions can only be investigated using EPMA and AES.

3.2. EPMA Analysis

EPMA element mapping was performed on both alloys in order to identify the phases as well as to quantify their volume fractions. The EPMA maps were collected from the entire coating thickness in a 100 μm wide section, near the centerline of the deposit, and image analysis of individual segments 0.5 mm in height was performed in order to quantify the volume of interdendritic areas and Cr-bearing particles. Element maps collected by EPMA in Fig. 4 show that there is a much higher volume fraction of Cr-rich particles in the Alloy B deposit. The variation in volume fractions of these regions through the thickness of each coating are shown in Figs. 5 and 6, which indicate the microstructures were nearly uniform through the thickness of the coating. The volume fraction of interdendritic phases (including the Cr particles) corresponds to about 35% in Alloy A, versus about 55% in Alloy B. The volume fraction of the Cr particles increased from about 1.5 to 15 vol.% in Alloy A versus B.

Figs. 3 and 4 show that a significantly higher volume fraction of Cr intermetallic phases were produced in Alloy B, and these were all situated within the interdendritic regions. From Figs. 2b and 4b, three morphologies of Cr particles could be distinguished in the coating produced from Alloy B, one consisting of a blocky equiaxed phase, another forming globular islands, and others taking on an acicular form with a rhombus-shaped cross-section.

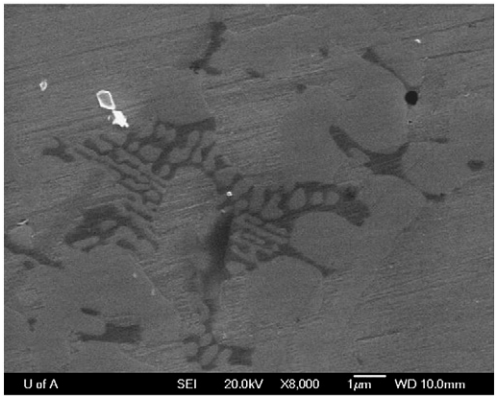

Fig. 3. SEM image of interdendritic region in Alloy B, with EDX quantification at location 7 corresponding with 86.2% Ni, 8.4% Si, 3.5% Cr, and 1.9% Fe, all in wt.%.

EPMA maps of B, C, Fe, Ni, and Si were also compared between the coatings. The maps of Si are shown in Fig. 7 which indicate that Si segregated preferentially to interdendritic regions forming a globular structure in both alloys, shown in detail in Fig. 3. The EPMA maps for other elements are shown in Fig. 8 for Alloy B. Boron also segregated preferentially to the interdendritic regions where it leads to the formation a significant fraction of chromium boride. Although the segregation of boron to interdendritic regions also occurred in Alloy A, few chromium borides could be detected. Carbon also segregated to interdendritic regions in both alloys, which accommodated the formation of Cr-carbides. The maps for boron and carbon in Fig. 8 suggest that the globular regions are Cr-carbides (with a lower carbon ratio than the acicular rhombus-shaped carbides), and the equiaxed globular regions are Cr-borides. It is interesting to note that in both alloys, the iron was concentrated in the primary dendrites.

An EPMA line scan across three Cr-bearing precipitates (located along the red arrow in Fig. 9) indicated that the rhombus-shaped precipitate was a chromium carbide and the two globular precipitates were chromium borides. This is consistent with the boron and carbon element maps showing globular or acicular Cr-carbides and nearly equiaxed Cr-borides in Fig. 8.

AES was used to quantify the compositions of various phases present in the deposit. This technique is highly surface sensitive, and only probes the first 10 nm of the sample which avoids interaction volume effects of the electron beam. The AES results for various point analyses (points B1–B12 in Fig. 9a) taken from Alloy B are shown in Table 3. The likely phases indicated by the AES results correlate well with previous data.

3.3. Microhardness and wear performance

The average hardness of the deposit made from Alloy B is about 600 HV (~55HRc) versus an average of 350 HV (~36HRc) for Alloy A (see Fig. 10). Both of these values are slightly higher than the nominal hardness values based on the manufacturer datasheets.

Microhardness measurements of individual phases were also obtained using a 25 g indenter load, and these are visible in Fig. 2. Several indents were made in the primary dendrite phases of Alloy A, which had an average hardness of 264 HV. The interdendritic phase of Alloy A had an average hardness of 500 HV, however individual Cr-based particles in this coating were too small for reliable hardness measurements to be obtained. Measurements of individual phases in Alloy B (see Fig. 11) reveals that the primary dendrite average hardness is about 405 HV with an average hardness for interdendritic region of 860 HV. In the case of Cr-based precipitates the hardness values ranged from 973 to 1400 HV, with an average of about 1200 HV.

Applying a composite model to the analysis of the hardness results, the average Vickers hardness of the coating can be expressed as:

$$HV = (V_d \times HV_d) + (V_{id} \times HV_{id}) + (V_p \times HV_p) \quad (1)$$

where V is the volume fraction, HV is the phase hardness (with subscripts "d", "id", and "p" representing dendritic, interdendritic, and Cr-particles, respectively) in the deposit. Based on the average measured values of the individual phases, the expected average hardness calculated from Eq. (1) is 348 HV for Alloy A, and 748 HV for Alloy B. These values are higher than the hardness values shown in Fig. 10 when testing with a 1 kg load. It is possible that this calculated average based on microhardness measurements may produce over-estimated values since particles with dimensions <25 μm were measured with microhardness testing, and this may result in hardness

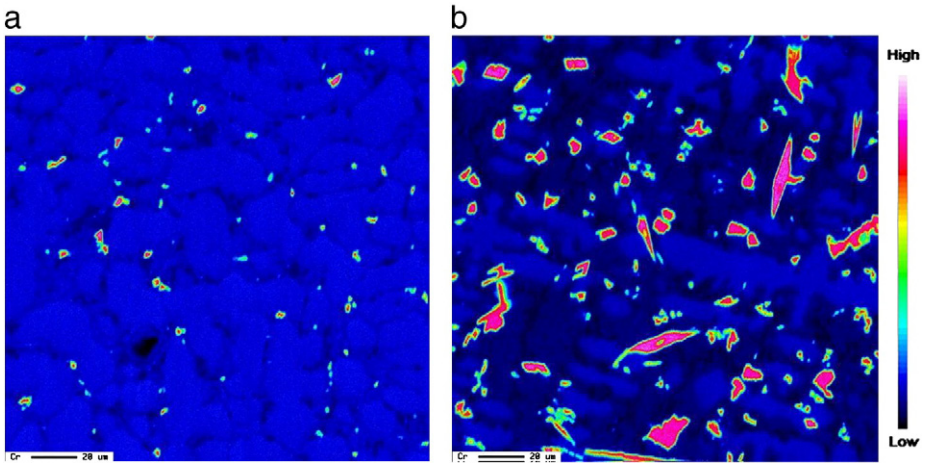

Fig. 4. EPMA Cr element map for (a) Alloy A, and (b) Alloy B, both obtained from the mid-thickness region.

overestimations due to possible strengthening effects at the surrounding particle/matrix interfaces. In addition, the thickness of softer phases may be less than the plastically deformed region produced during indentation and thus lead to overestimated predictions using Eq. (1). However, this composite model appears to give a reasonable prediction of the average hardness based on the volume fractions of the various phases.

Wear testing as per ASTM G65 indicated that wear resistance was consistent with the hardness, with Alloy A having a mass loss of 1.862 g, and Alloy B having a mass loss of 0.546 g after 6000 revolutions of the abrasive wheel. This can be correlated to the higher volume fraction of harder phases (interdendritic regions and carbides) present in Alloy B which contributes to the higher average hardness.

4. Discussion

4.1. Microstructural constituents

The microstructures of the deposits for both alloys were nearly uniform through their thickness. This in contrast to earlier findings regarding NiCrBSi PTAW deposits on stainless steel [3] which consisted of 3 distinct regions with different microstructures and hardness values. The present EPMA results indicate nearly uniform microstructures and macrohardness values throughout the deposit, and it is likely that lower base material dilution accounts for the through-thickness uniformity. Alloy B showed the higher interdendritic/intermetallic volume fractions because there is more carbon and boron, which segregate to the interdendritic areas (since their solubility in Ni is negligible) and lead to the formation of hard phases such as carbides and borides. Optical and SEM imaging indicated that during PTAW of a NiCrBSi alloy, Cr-borides formed first, followed by Ni solid solution simultaneously with the growth of Cr-carbides, and the remaining liquid forming a Ni–Ni_3B eutectic [10].

EPMA element maps and line scans of both alloys showed that silicon and boron segregated to the interdendritic regions and may be forming γNi–Ni_3Si eutectic, along with Ni_3B, however, previous work using a high power laser diode also indicated the presence of Ni_3Fe [11]. In that case laser cladding produces a much thinner coating which drastically reduces the diffusion distance required for iron from the substrate into the coating. One may expect that iron diffusion and Ni_3Fe formation should be limited to within the first 0.5 mm of the coating interface based on the previous results.

AES results in Table 3 indicate the presence of Cr_3C_2 (points B1–B3), Cr_7C_3(points B4 and B5), CrB (points B6–B8), and Ni_3B phases (points B9–B12) in the interdendritic regions, see Fig. 9(a). These results are consistent with previous work, however Cr_2B has also been reported in other studies [3]. The AES quantifications also indicate that in terms of carbide particle shape, the rhombus-shaped carbides were most likely Cr_3C_2 and the irregular shaped carbides are Cr_7C_3 particles.

The wear resistance of NiCrBSi coatings is largely attributed to the formation of hard boride and carbide particles [3]. For example, the hardness of Cr_2B particles is about 1250 HV [12] and 1400 HV and 1700 HV for Cr_3C_2 and Cr_7C_3, respectively [13]. However, in the present work, AES analysis suggests that approximately half of the Cr-based particles are CrB. The formation of CrB may actually be

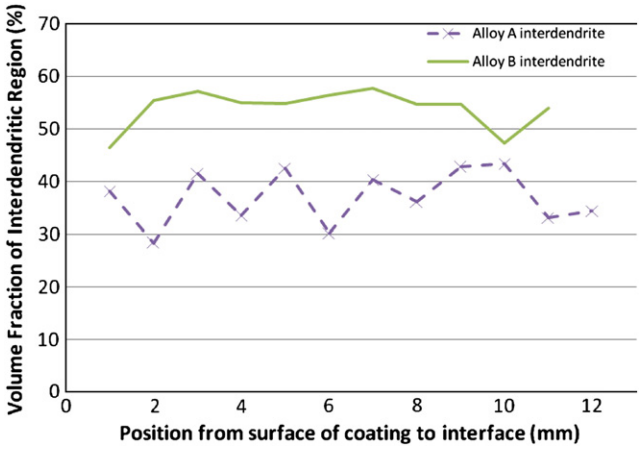

Fig. 5. Volume fraction of interdendritic regions for alloys A and B.

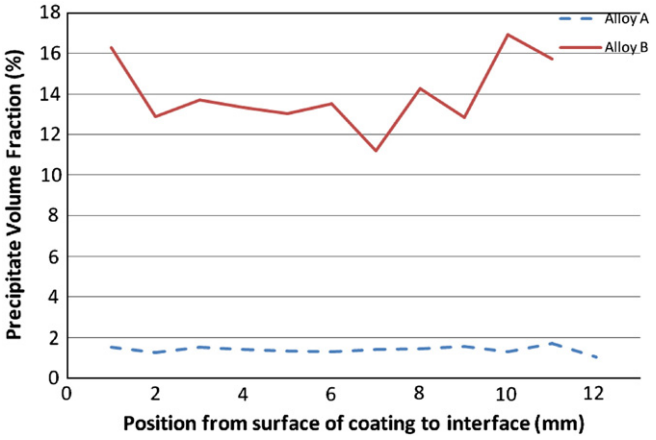

Fig. 6. Volume fractions of Cr particles in alloys A and B.

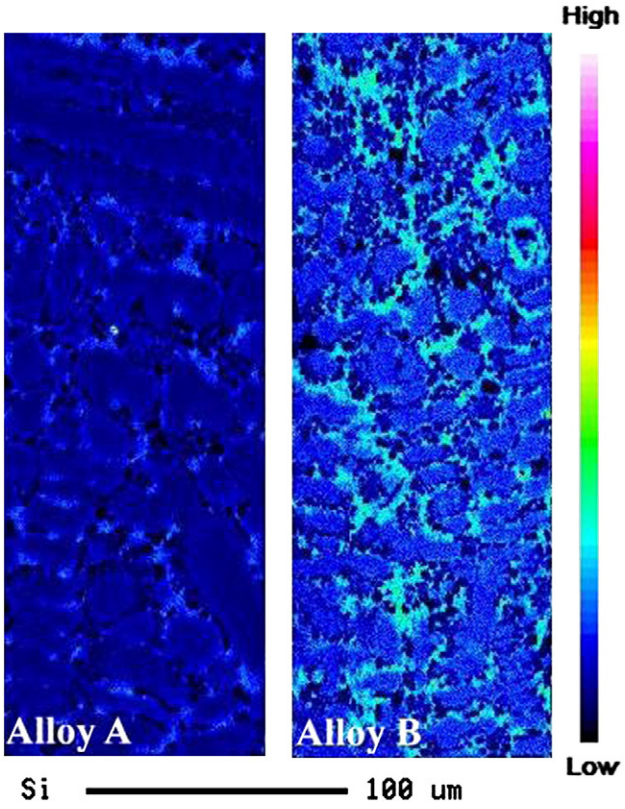

Fig. 7. EPMA maps of Si in alloys A and B.

preferred in terms of optimizing coating performance since it has a hardness of 2300 HV [14]. From the EPMA carbon element map of Alloy B (see Fig. 8), it can be seen that there are carbides with differing carbon counts which is likely due to different chromium carbide phases.

4.2. Element segregation

Since the solubility of C, B and Si is very low in the γ-Ni phase, the addition of these elements leads to their segregation towards the interdendritic regions as shown in Figs. 3 and 7. However, the segregation of Cr has seldom been considered in the NiCrBSi system, yet this is an important element since the formation of Cr-borides and carbides is controlled by the Cr concentration at the interdendritic regions where the C and B are concentrated. Although there is only a slight increase in the Cr content from Alloy A to Alloy B, there is a substantial increase in the amount of Cr particles produced. The influence of alloy composition on elemental segregation can be understood from the viewpoint of solidification theory and the Scheil equation which states that the composition of the solid at the solid/liquid interface is [15]:

$$C_s^* = kC_o[1-f_s]^{k-1} \tag{2}$$

where C_o is the nominal composition of the alloy, f_s is the fraction of solid, and k is referred to as the segregation coefficient which corresponds with the ratio C_s/C_l between the composition of the solid and the composition of the liquid. In the case of the partitioning of elements, values of $k<1$ indicate low solubility for the element and rejection of it away from the dentrite core, and values of $k>1$ indicate high solubility within the dendrite. It has been shown that the

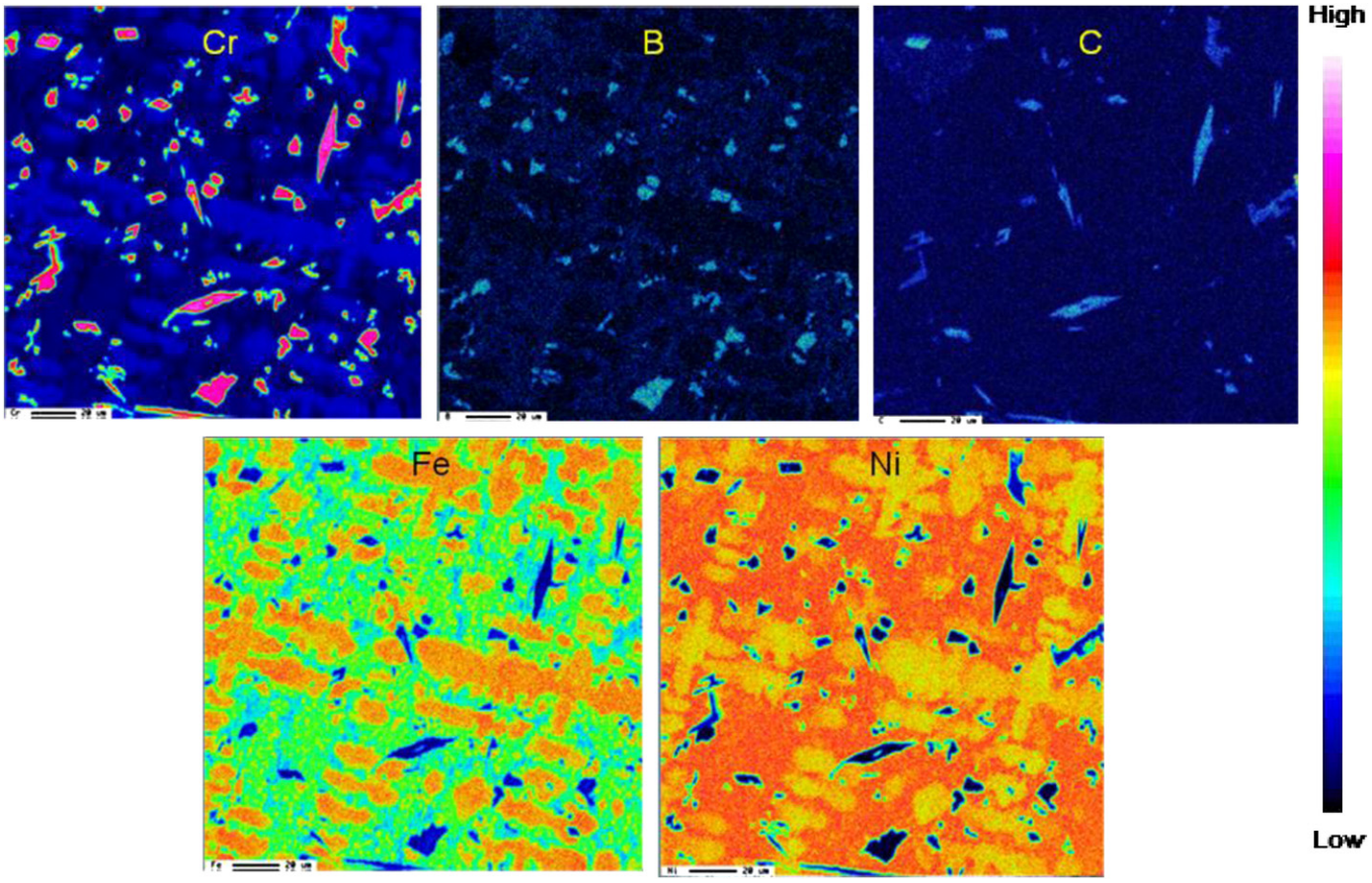

Fig. 8. EPMA map of Cr, B, C, Fe and Ni regions in Alloy B.

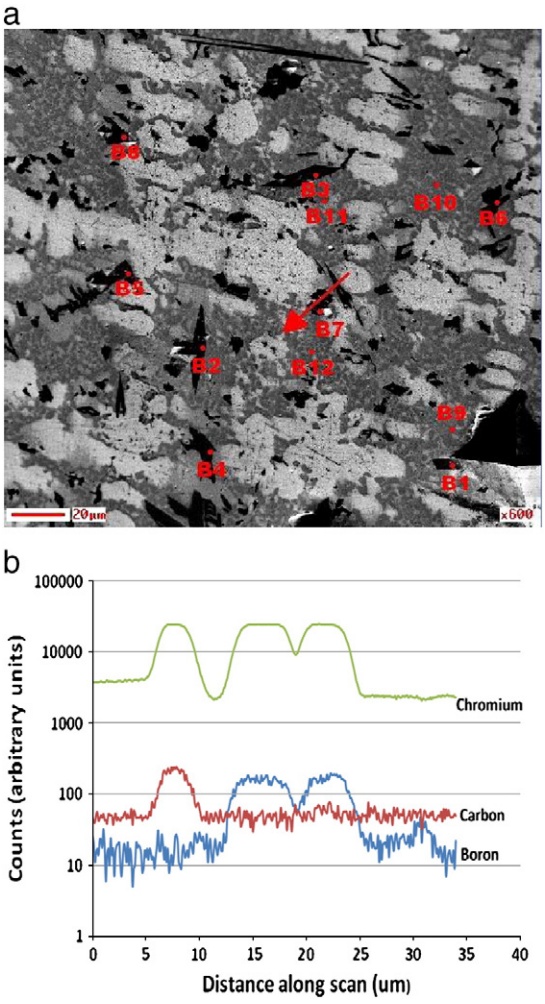

Fig. 9. (a) Line scan across selected area highlighted by red arrow in Alloy B. (b) WDX intensity measurements along the arrow indicated in Fig. 9(a).

application of the Scheil equation is valid during arc welding processes, since there is negligible diffusion in the solid, perfect mixing in the liquid, and undercooling is not significant [16].

Since the start of solidification occurs when f_s is zero, Dupont et. al showed that composition data obtained by EDX point analysis for the cores of dendrites can be used to quantify segregation via the Scheil equation [16]. In this case, the EDX quantification was averaged from at least 5 dendrites to yield values for C_s, and this is compared to the average composition of the deposits C_o, obtained by inductively

Table 3
AES results for Alloy B.

Point	Atomic percent						Probable phase
	C	Cr	B	Ni	Fe	Si	
B1	44.8	54.9	0	0.3	0	0	Cr_3C_2
B2	44.6	54.7	0	0.2	0.6	0	Cr_3C_2
B3	45.2	54.8	0	0	0	0	Cr_3C_2
B4	33.9	54.9	2.7	5.7	2.8	0	Cr_7C_3
B5	38.2	54	1.9	4.6	1.3	0	Cr_7C_3
B6	0.5	54.3	45.2	0	0	0	CrB
B7	7.5	50	41.2	0.4	0.9	0	CrB
B8	0.2	52.5	47	0.3	0	0	CrB
B9	0	7.2	29.1	62.7	0	0.9	Ni_3B
B10	2.3	4.5	29.4	63.8	0	0	Ni_3B
B11	7.6	3.9	21.4	63.4	0	3.8	Ni_3B/Ni_3Si
B12	4.7	5.1	14.1	68	0	8	Ni_3B/Ni_3SiSi

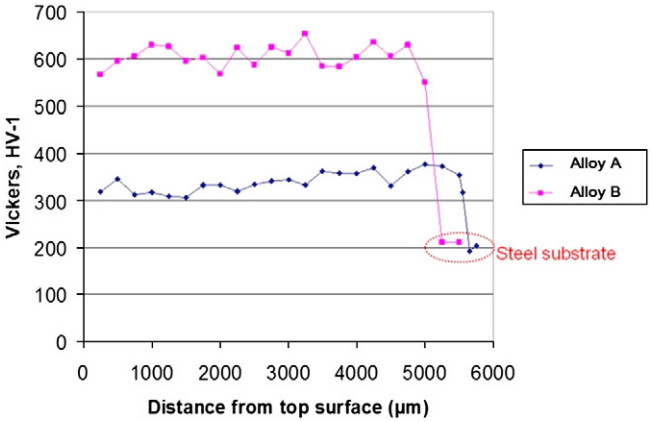

Fig. 10. Hardness profiles in alloys A and B through the coating thickness.

coupled plasma (ICP) analysis shown in Table 4. This table shows the segregation coefficient value k (where lower values suggest more segregation away from the dendrite core) for the elements in both alloys. Comparing the segregation coefficient values in both Alloys A and B, it can be seen that there is a tendency for the Cr to segregate slightly towards the dendrite in both alloys. This situation is not desirable from the perspective of optimizing wear performance, since hardness and wear resistance improves with the formation of Cr-borides and Cr-carbides. Considering that EPMA maps for Alloy B indicate that a considerable amount of boron is concentrated in the interdendritic regions (see Fig. 8), any alloy additions which could promote the segregation of Cr away from the γ-Ni dendrites (rather than toward the dendrite) are desirable. The values for carbon and boron have been neglected in the analysis in Table 4, since quantification of each of these elements at values of <1% by SEM methods are not feasible. However this does not have a significant effect on the other k values presented in Table 4, as the combined fraction of C, and B is <2.4 wt.% in both alloys.

An examination of the ternary phase diagrams for both the Ni–Cr–Fe and Ni–Cr–Si systems reveals that addition of both Fe and Si will reduce the solubility of Cr in the γNi phase, and hence promote Cr segregation to the interdendritic area. However, since the increase of Fe was from 2.70 to 4.49 wt.% in Alloy A versus Alloy B, the relative change in the Cr solubility was not significant enough to promote Cr segregation to interdendritic regions. The fraction of Si did not significantly change in the two alloys, and the Si itself had a strong tendency to segregate away from the dendrites. This would suggest a much greater increase in Si would be required to promote Cr segregation compared to additions of iron. Since the iron itself preferentially segregates to the γ-Ni dendrites, it has a greater potential to change the Cr solubility in the solidifying dendrite [17]. This could promote segregation of Cr to the boron-rich interdendritic regions, and enhance the rate of Cr-boride formation. In

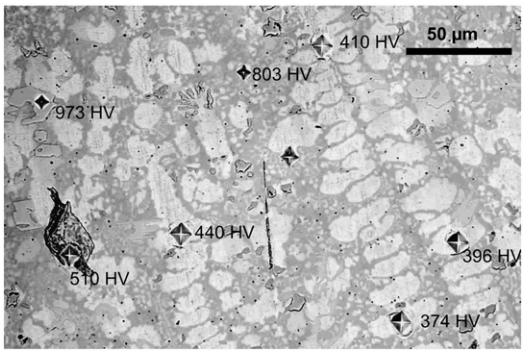

Fig. 11. Microhardness measurements of selected area in Alloy B.

Table 4
Segregation coefficient "*k*" for elements in overlay deposits.

Element (wt%)	Deposit ICP analysis, C_o	Dendrite core	*k*
Alloy A			
Ni	Bal	85.49	–
Fe	2.70	3.09	1.14
B	1.25	–	–
C	0.11	–	–
Cr	8.63	9.62	1.11
Si	3.14	1.8	0.57
Alloy B			
Ni	Bal.	81.21	–
Fe	4.49	5.59	1.24
B	1.98	–	–
C	0.42	–	–
Cr	9.28	10.71	1.15
Si	3.94	2.48	0.63

the case of the two alloys studied, the contribution of additional Fe to segregation of Cr only had a minor influence within the composition range examined.

4.3. Factors influencing hardness

The average hardness calculated from Eq. (1) is higher than the average hardness shown in Fig. 10. This is likely to be higher due the small size of the regions which are probed during indentation. For example, since the size of the plastic zone may approach or exceed the dimensions of the soft dendritic regions, the apparent hardness of dendrites may be higher than the actual value since these phases are surrounded by a significantly harder interdendritic region containing intermetallic phases. Also, the plastic zone may encounter interphase boundaries which would provide a hardening effect. Although these considerations regarding the plastic interaction volume should be taken into account, it is clear that the boron and silicon-rich interdendritic regions provide a major contribution to the hardness, particularly in Alloy B, since formation of Ni_3B and Ni_3Si occur which have hardness values of approximately 1000 and 600 HV respectively [18,19].

The role of B and Si in the alloy chemistry has traditionally been recognized as melting point suppressants [9]. In the case of Si, this is accomplished by the formation of a γNi-Ni_3Si eutectic with a melting point expected at 1143 °C based on the binary phase diagram [17]. Since Fig. 3 indicates that these phases are primarily formed in the interdendritic regions during terminal solidification, the addition of Si will increase their volume fraction and the overall hardness of the alloy. This effect is enhanced by the fact that Si also segregates away from the γ-Ni dendrites during the initial stages of solidification.

The present work has shown that B and Si both segregate to interdendritic regions, see Figs. 7 and 8. Due to the very limited solubility of boron in Ni, it is likely to have a dominant role in determining the volume fraction of the interdendritic region. For example, the boron content increases from 1.25 to 1.98 wt.% in Alloy A versus B. One may expect Alloy B to contain both a higher interdendritic and intermetallic volume fraction since there is more boron and carbon which segregate to the interdendritic areas and form the hard phases such as Cr-carbides, and borides. Although the formation of hard CrB phases primarily occurs in the interdendritic regions, this may have been inhibited by the formation of γNi–Ni_3B eutectic during terminal solidification. Following the solidification, the nucleation and growth of CrB is much slower due to the low diffusion rate in the solid state. The formation of CrB is also inhibited by the segregation of Cr towards the dendrite core, reducing the amount of Cr available at interdendritic regions (see Figs. 2 and 3).

5. Conclusions

It was found that the hardness of a typical NiCrBSi alloy deposit was controlled not only by the amount of Cr-rich particles present but also by the volume fraction of the interdendritic phase. The interdendritic phase was shown to exhibit high hardness of about 860 HV relative to the primary dendritic phase which had a hardness of 405 HV. Since the volume fraction of the interdendritic phases is higher for the harder alloy (~55% in Alloy B), it significantly contributes to the overall properties of the deposit.

Although there was only a minor increase in Cr, C, and B content in Alloy B, this lead to a large increase in the amount of Cr-particles from 1.5 to about 15 vol.% between the two alloys examined. Ternary phase diagrams suggest the addition of Fe or Si will decrease the solubility of Cr in Ni, however no significant change Cr segregation was observed in the alloy compositions examined. It was also found that boron segregates to the interdendritic regions in both alloys and promotes formation of Ni_3B and CrB.

References

[1] D.J. Branagan, M.C. Marshall, B.E. Meacham, Mater. Sci. Eng. A 428 (2006) 116.
[2] N.Y. Sari, M. Yilmaz, Surf. Coat. Technol. 202 (2008) 3136.
[3] C. Sudha, P. Shankar, R.V.S. Rao, R. Thirumurugesan, M. Vijayalakshmi, B. Raj, Surf. Coat. Technol. 202 (2008) 2103.
[4] E. Gruzdys, S. Meskinis, S. Tamulevicius, T. Grinys, Mater. Sci. 14 (2008) 4.
[5] T. Gómez-del Río, M.A. Garrido, J.E. Fernández, M. Cadenas, J. Rodríguez, J. Mater. Process. Technol. 204 (2008) 304.
[6] J.F. Flores, A. Neville, N. Kapur, A. Gnanavelu, Wear 267 (2009) 213.
[7] C. Navas, R. Vijande, J.M. Cuetos, M.R. Fernández, J. de Damborenea, Surf. Coat. Technol. 201 (2006) 776.
[8] M. Yarmuch, in: Chemical and Materials Engineering, University of Alberta, Edmonton, 2005 201 pp.
[9] E. Badisch, M. Kirchgaßner, Surf. Coat. Technol. 202 (2008) 6016.
[10] H.J. Kim, Y.J. Kim, Surf. Eng. 15 (1999) 495.
[11] A. Conde, F. Zubiri, J. de Damborenea, Mater. Sci. Eng. A 334 (2002) 233.
[12] D. Nam, J. Do, S. Lee, Scr. Mater. 60 (2009) 695.
[13] D. Nam, K. Lee, S. Lee, Metall. Mater. Trans. A 39 (2008) 2626.
[14] M. Bauccio, ASM Engineered Materials Reference Book, 2nd ed., ASM International, Materials Park, OH, 1994.
[15] E. Scheil, Z. Metallkd. 34 (1942) 70.
[16] J.N. Dupont, J.R. Michael, B.D. Newbury, Weld. J. 78 (1999) 408s.
[17] ASM Handbook Committee, ASM Handbook Comprehensive Index, 2nd ed., ASM International, Materials Park, Ohio, 2000.
[18] C.B. Finch, O.B. Cavin, P.F. Becher, J. Cryst. Growth 67 (1984) 556.
[19] S. Milenkovic, R. Caram, J. Cryst. Growth 237–239 (2002) 95.